PHYSICAL REVIEW E **91**, 053020 (2015)

Compressible turbulent mixing: Effects of Schmidt number

Qionglin Ni[*]
State Key Laboratory for Turbulence and Complex Systems, College of Engineering, Peking University, 100871, Beijing, People's Republic of China
and Department of Physics, University of Rome Tor Vergata, Via della Ricerca Scientifica 1, 00133, Rome, Italy

(Received 11 February 2015; published 26 May 2015)

We investigated by numerical simulations the effects of Schmidt number on passive scalar transport in forced compressible turbulence. The range of Schmidt number (Sc) was $\frac{1}{25} \sim 25$. In the inertial-convective range the scalar spectrum seemed to obey the $k^{-5/3}$ power law. For $\mathrm{Sc} \gg 1$, there appeared a k^{-1} power law in the viscous-convective range, while for $\mathrm{Sc} \ll 1$, a $k^{-17/3}$ power law was identified in the inertial-diffusive range. The scaling constant computed by the mixed third-order structure function of the velocity-scalar increment showed that it grew over Sc, and the effect of compressibility made it smaller than the $\frac{4}{3}$ value from incompressible turbulence. At small amplitudes, the probability distribution function (PDF) of scalar fluctuations collapsed to the Gaussian distribution whereas, at large amplitudes, it decayed more quickly than Gaussian. At large scales, the PDF of scalar increment behaved similarly to that of scalar fluctuation. In contrast, at small scales it resembled the PDF of scalar gradient. Furthermore, the scalar dissipation occurring at large magnitudes was found to grow with Sc. Due to low molecular diffusivity, in the $\mathrm{Sc} \gg 1$ flow the scalar field rolled up and got mixed sufficiently. However, in the $\mathrm{Sc} \ll 1$ flow the scalar field lost the small-scale structures by high molecular diffusivity and retained only the large-scale, cloudlike structures. The spectral analysis found that the spectral densities of scalar advection and dissipation in both $\mathrm{Sc} \gg 1$ and $\mathrm{Sc} \ll 1$ flows probably followed the $k^{-5/3}$ scaling. This indicated that in compressible turbulence the processes of advection and dissipation except that of scalar-dilatation coupling might deferring to the Kolmogorov picture. It then showed that at high wave numbers, the magnitudes of spectral coherency in both $\mathrm{Sc} \gg 1$ and $\mathrm{Sc} \ll 1$ flows decayed faster than the theoretical prediction of $k^{-2/3}$ for incompressible flows. Finally, the comparison with incompressible results showed that the scalar in compressible turbulence with $\mathrm{Sc} = 1$ lacked a conspicuous bump structure in its spectrum, but was more intermittent in the dissipative range.

DOI: 10.1103/PhysRevE.91.053020 PACS number(s): 47.40.−x, 47.10.ad, 47.27.Gs

I. INTRODUCTION

Turbulent mixing is of importance in many fields including the scattering of interstellar materials throughout the Universe, the dispersion of air pollutants in the atmosphere, and the combustion of chemical reactions within an engine [1–6]. In the literature of fluid dynamics, mixing in turbulent flows is often called a scalar turbulence. The related classical picture of cascade is that scalar fluctuations are generated at large scales and transported through successive breakdowns into smaller scales; the process proceeds until the scalar fluctuations are homogenized and dissipated by molecular diffusion at the smallest scale. Therefore, how a scalar gets mixed by a flow depends on whether its molecular diffusivity is small or large, even if the flow is fully turbulent. The common measure of diffusivity is based on the Schmidt number $\mathrm{Sc} \equiv \nu/\chi$, where ν and χ are the kinematic viscosity and molecular diffusivity, respectively. Generally, there are three different Sc regimes in turbulent mixing. For $\mathrm{Sc} \simeq 1$, previous experiments and simulations [7–9] have suggested that the scalar spectrum in the inertial-convective range follows the $k^{-5/3}$ power law when the Reynolds number is sufficiently high. The weakly diffusive regime ($\mathrm{Sc} \gg 1$) has also received great deal of attention [10–12], especially concerning the k^{-1} power law for the spectral roll-off in the viscous-convective range [13]. In terms of the strongly diffusive regime ($\mathrm{Sc} \ll 1$), recent simulations [14,15] have provided strong support for the putative theory proposed by Batchelor, Howells, and Townsend (hereafter referred to as BHT) [16]; namely, that the scalar spectrum in the inertial-diffusive range obeys the $k^{-17/3}$ power law.

As is well known, compressible turbulence is crucial to a large number of industrial applications and natural phenomena, such as the design of transonic and hypersonic aircraft, interplanet space exploration, solar winds, and star-forming clouds in a galaxy. Nevertheless, our current understanding of scalar transport in compressible turbulent flows lags far behind the knowledge accumulated on the incompressible one. Previous simulations of mixing in compressible turbulence using the piecewise-parabolic method [17,18] showed that for velocity, the compressive component is less efficient in enhancing mixing than the solenoidal component. Moreover, the scaling of scalar structure function accords well with the SL94 model. In this paper, we carried out a series of numerical simulations for compressible turbulent mixing, using a novel computational approach [19]. To examine in detail the effects of the Schmidt number on the scalar transport in compressible turbulence, the turbulent Mach number was fixed at around 0.30, whereas the Taylor microscale Reynolds and Schmidt numbers were varied from 34 to 216 and $\frac{1}{25}$ to 25, respectively. For focusing the influences brought by shock waves, a large-scale forcing with overwhelming compressive component is added to drive and maintain the velocity field [20]. This paper is part of a systemic investigation of the effects of basic parameters on compressible turbulent mixing. In a companion paper [21], we carefully examined the effects caused by changes in the Mach number and forcing scheme.

---

[*] niql.pku@gmail.com

©2015 American Physical Society

The rest of this paper is organized as follows: The governing equations and simulated parameter, along with the computational method used, are presented in Sec. II. In Sec. III, we first analyze the spectrum and structure function, then describe the probability distribution function, and finally discuss the scalar transport in $\mathrm{Sc} \gg 1$ and $\mathrm{Sc} \ll 1$ flows. The summary and conclusions regarding this paper are given in Sec. IV.

II. GOVERNING EQUATIONS AND SIMULATION PARAMETERS

We consider a statistically stationary system of a passive scalar advected by the compressible turbulence of an idea gas. The velocity and scalar fields are driven and maintained by large-scale velocity and scalar forcings, respectively, where in the former the ratio of compressive to solenoidal components for each wave number is $20:1$. Furthermore, the accumulated internal energy at small scales is removed by cooling function at large scales. By introducing the basic scales of L for length, ρ_0 for density, U for velocity, T_0 for temperature, and ϕ_0 for scalar, we obtain the dimensionless form of governing equations, plus the dimensionless state equation of ideal gas, as follows:

$$\frac{\partial \rho}{\partial t}+\frac{\partial(\rho u_j)}{\partial x_j}=0, \tag{2.1}$$

$$\frac{\partial(\rho u_i)}{\partial t}+\frac{\partial[\rho u_i u_j+p\delta_{ij}/\gamma M^2]}{\partial x_j}=\frac{1}{\mathrm{Re}}\frac{\partial \sigma_{ij}}{\partial x_j}+\rho\mathcal{F}_i, \tag{2.2}$$

$$\begin{aligned}\frac{\partial \mathcal{E}}{\partial t}&+\frac{\partial[(\mathcal{E}+p/\gamma M^2)u_j]}{\partial x_j}\\ &=\frac{1}{\alpha}\frac{\partial}{\partial x_j}\left(\kappa\frac{\partial T}{\partial x_j}\right)+\frac{1}{\mathrm{Re}}\frac{\partial(\sigma_{ij}u_i)}{\partial x_j}-\Lambda+\rho\mathcal{F}_j u_j,\end{aligned} \tag{2.3}$$

$$\frac{\partial(\rho\phi)}{\partial t}+\frac{\partial[(\rho\phi)u_j]}{\partial x_j}=\frac{1}{\beta}\frac{\partial}{\partial x_j}\left(\rho\chi\frac{\partial\phi}{\partial x_j}\right)+\rho\mathcal{S}, \tag{2.4}$$

$$p=\rho T. \tag{2.5}$$

The primary variables are the density ρ, velocity vector $\mathbf{u}$, pressure p, temperature T, and scalar ϕ. The nondimensional parameters α and β are $\alpha=\mathrm{PrRe}(\gamma-1)M^2$ and $\beta=\mathrm{ScRe}(\gamma-1)\gamma$. $\mathcal{F}_j$ is the dimensionless large-scale velocity forcing,

$$\mathcal{F}_j=\sum_{l=1}^{2}\hat{\mathcal{F}}_j(\mathbf{k}_l)\exp(i\mathbf{k}_l\mathbf{x})+\mathrm{c.c.}, \tag{2.6}$$

where $\hat{\mathcal{F}}_j$ is the Fourier amplitude, it has a solenoidal component perpendicular to $\mathbf{k}_l$ and a compressive component parallel to $\mathbf{k}_l$, and in magnitude the latter is twenty times greater than the former. Similarly, the dimensionless large-scale scalar forcing $\mathcal{S}$ is written as

$$\mathcal{S}=\sum_{l=1}^{2}\hat{\mathcal{S}}(\mathbf{k}_l)\exp(i\mathbf{k}_l\mathbf{x})+\mathrm{c.c.} \tag{2.7}$$

However, there is only a solenoidal component in $\hat{\mathcal{S}}$. The details of the thermal cooling function Λ can be found in Ref. [19]. The viscous stress σ_{ij} and total energy per unit volume $\mathcal{E}$ are defined by

$$\sigma_{ij}\equiv\mu\left(\frac{\partial u_i}{\partial x_j}+\frac{\partial u_j}{\partial x_i}\right)-\frac{2}{3}\mu\theta\delta_{ij}, \tag{2.8}$$

$$\mathcal{E}\equiv\frac{p}{(\gamma-1)\gamma M^2}+\frac{1}{2}\rho(u_j u_j). \tag{2.9}$$

Here, $\theta=\partial u_k/\partial x_k$ is the velocity divergence or dilatation. $M\equiv U/c_0$ is the reference Mach number and $c_0\equiv\sqrt{\gamma R T_0}$ is the reference sound speed, where R is the specific gas constant, and $\gamma\equiv C_p/C_v$ is the ratio of specific heat at constant pressure C_p to that at constant volume C_v. We shall assume that both specific heats are independent of temperature, which is a reasonable assumption for the air temperature in the simulation of the current Mach number [19]. By adding the reference dynamical viscosity μ_0, thermal conductivity κ_0, and molecular diffusivity χ_0, we obtain three additional governing parameters: the reference Reynolds number $\mathrm{Re}\equiv\rho_0 UL/\mu_0$, the reference Prandtl number $\mathrm{Pr}\equiv\mu_0 C_p/\kappa_0$, and the reference Schmidt number $\mathrm{Sc}\equiv\nu_0/\chi_0$, where $\nu_0\equiv\mu_0/\rho_0$ is the reference kinematic viscosity. In the current study the values of γ and Pr are set as 1.4 and 0.7, respectively. Thus, there remain three independent parameters of M, Re, and Sc to govern the system. For completion, we employ the Sutherland law to specify the temperature-dependent dynamical viscosity, thermal conductivity, and molecular diffusivity as follows:

$$\mu,\kappa,\chi=\frac{1.4042T^{1.5}}{T+0.4042}. \tag{2.10}$$

The system is solved numerically in a cubic box with periodic boundary conditions by adopting a new computational method. This method utilizes a seventh-order weighted essentially nonoscillatory (WENO) scheme [22] for shock regions and an eighth-order compact central finite difference (CCFD) scheme [23] for smooth regions outside shocks. A flux-based conservative formulation is implemented to optimize the treatment of interface between the two regions and then improve the computational efficiency. The details have been described in Ref. [19]. Instead of M and Re, the compressible flow is directly governed by the turbulent Mach number M_t and the Taylor microscale Reynolds number (Re_λ) [24], which are defined as follows:

$$M_t\equiv M\frac{u'}{\langle\sqrt{T}\rangle}, \tag{2.11}$$

$$\mathrm{Re}_\lambda\equiv\mathrm{Re}\frac{u'\lambda\langle\rho\rangle}{\sqrt{3}\langle\mu\rangle}, \tag{2.12}$$

where $u'\equiv(\langle u_j^2\rangle)^{1/2}$ and $\lambda\equiv u'/[\langle(\partial u_j/\partial x_j)^2\rangle]^{1/2}$ are the root-mean-square (r.m.s.) velocity magnitude and the Taylor microscale, respectively. The sign $\langle\cdot\rangle$ denotes the ensemble average and the repetition on the subscript stands for Einstein summation. Here, we point out that the definitions of M_t and Re_λ are based on nondimensional variables, which is continuously used in the following text if there is no special illustration.

Table I presents the major simulation parameters. The simulations are conducted on a $N^3=512^3$ grid and divided into two groups according to the value of Re_λ. The first

TABLE I. Flow statistics in the simulations.

Case	Sc	M_t	Re_λ	η	η_B	η_{OC}	u'	ϕ'	E_K	E_ϕ	$\langle\epsilon\rangle$	$\langle\epsilon_\phi\rangle$	r_ϕ
C1	25	0.28	35	0.027	0.005		2.06	2.75	2.13	3.81	1.20	0.80	0.37
C2	5	0.28	35	0.027	0.012		2.06	2.44	2.15	3.00	1.19	0.87	0.52
C3	1	0.28	34	0.027	0.027		2.06	2.14	2.11	2.30	1.21	0.92	0.70
C4	1	0.29	208	0.007		0.007	2.11	2.24	2.28	2.53	0.41	0.90	1.98
C5	$\frac{1}{5}$	0.29	207	0.007		0.023	2.11	2.11	2.24	2.25	0.40	0.93	2.31
C6	$\frac{1}{25}$	0.30	216	0.007		0.078	2.15	1.98	2.30	1.97	0.43	1.25	3.40

group including C1, C2, and C3 is used to study scalars with low molecular diffusivity in low Re flows, where Sc is decreased from 25, 5, to 1, and Re_λ is around 35. For the three cases, the smallest scale for velocity is the Kolmogorov scale $\eta \equiv [\langle\mu/(\text{Re}\rho)\rangle^3/\langle\epsilon/\rho\rangle]^{1/4}$, and that for the scalar is the Batchelor scale $\eta_B = \text{Sc}^{-1/2}\eta$ with values of 0.005, 0.012, and 0.027. In the second group addressing C4, C5, and C6, we pay attention to scalars with high molecular diffusivity in high Re flows, where Sc is decreased from 1, $\frac{1}{5}$, and $\frac{1}{25}$, and Re_λ is around 210. Here, the smallest scale for a scalar is the Corrsin scale, $\eta_C = \text{Sc}^{-3/4}\eta$, instead of the Batchelor scale, η_B, with values of 0.007, 0.023, and 0.078.

The r.m.s. magnitude of velocity u' and the kinetic energy per unit volume E_K are increased by Re_λ rather than by Sc. In contrast, the r.m.s. magnitude of scalar ϕ' and the scalar variance per unit volume E_ϕ mainly grow with Sc in both high and low Re flows, where the related definitions are $\phi' \equiv (\langle\phi^2\rangle)^{1/2}$, $E_K \equiv \langle\rho u_j^2\rangle/2$, and $E_\phi \equiv \langle\rho\phi^2\rangle/2$. Because M_t is fixed, the ensemble-average value of the kinetic-energy dissipation rate $\langle\epsilon\rangle$ becomes only dependent on Re_λ. In contrast, that of the scalar dissipation rate $\langle\epsilon_\phi\rangle$ in both high- and low-Re flows increases as Sc decreases. Here, $\epsilon \equiv \sigma_{ij}S_{ij}/\text{Re}$, $\epsilon_\phi \equiv \chi(\partial\phi/\partial x_j)^2$, and $S_{ij} = (\partial u_i/\partial x_j + \partial u_j/\partial x_i)/2$ is the strain rate tensor. For the ratio of the mechanical to scalar timescales $r_\phi = (\langle\rho\mathbf{u}^2/2\rangle/\langle\epsilon\rangle)/(\langle\rho\phi^2/2\rangle/\langle\epsilon_\phi\rangle)$, its dependence on Sc is similar to that of $\langle\epsilon_\phi\rangle$.

Furthermore, an alternative to r_ϕ is the quantity of $f_\phi = (L_f/u')/(\langle\rho\phi^2/2\rangle/\langle\epsilon_\phi\rangle)$, where L_f is the integral length scale [25]. In Fig. 1 we plot f_ϕ against the logarithm of the product of Re_λ and Sc. It shows that f_ϕ falls monotonically when the product increases.

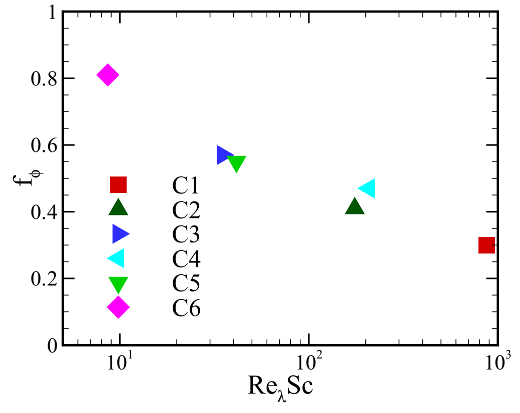

FIG. 1. (Color online) Normalized scalar dissipation rate versus the product of Re_λ and Sc.

III. SIMULATION RESULTS

A. Spectrum and structure function

By applying the Kolmogorov theory [26,27] to the scalar transport in incompressible turbulent flows, Obukhov [28] and Corrsin [29] derived a scalar spectrum in the inertial-convective range satisfying $L_\phi^{-1} \ll k \ll \eta^{-1}$:

$$E_\phi(k) = C_\phi\langle\epsilon_\phi\rangle\langle\epsilon\rangle^{-1/3}k^{-5/3}, \tag{3.1}$$

where L_ϕ is the integral length scale of scalar [25]. C_ϕ is the Obukhov–Corrsin (OC) constant, and the typical values are 0.75 ~ 0.92 by experiment and 0.87 ± 0.10 by simulation [8,30]. In Fig. 2 we plot the compensated spectra of scalar according to the OC variables at different Sc and Re_λ. For the curves of $E_\phi(k)$, plateaus appear in the inertial-convective ranges, especially for the Sc = 1 flows. This means that, in the range $L_\phi^{-1} \ll k \ll \eta^{-1}$, the scalar spectrum in compressible turbulent mixing seems to also obey the $k^{-5/3}$ power law. In high-Sc flows, $E_\phi(k)$ in the regime between the inertial-convective and dissipative ranges grows with wave number, which is reinforced by the increase in Sc. Contrarily, in low-Sc flows, in the same regime $E_\phi(k)$ falls as wave number increases, and this behavior is enhanced by the decrease in Sc. It implies that in a certain range, the scalar spectrum in a low- or high-Sc flow may have additional scaling.

Although it is straightforward to compute in simulations the three-dimensional (3D) scalar spectrum as a function of wave number, experiments usually measure only the one-dimensional (1D) version of $E_{1\phi}(k)$. In isotropic turbulence, it

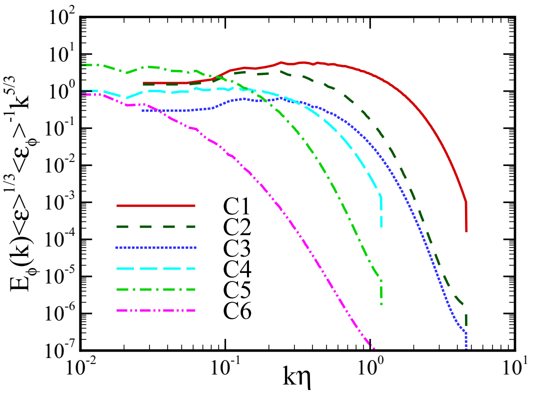

FIG. 2. (Color online) Compensated spectrum of scalar according to the Obukhov–Corrsin variables at different values of Sc and Re_λ.

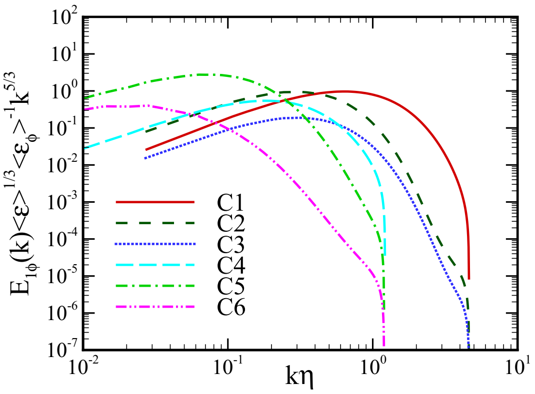

FIG. 3. (Color online) One-dimensional compensated spectrum of scalar at different values of Sc and Re_λ.

is written as

$$E_{1\phi}(k) = -\int_k^\infty \frac{E_\phi(k)}{k}dk. \tag{3.2}$$

Figure 3 presents the 1D compensated scalar spectra at different Sc and Re_λ. We have taken averages over three coordinate directions. Previous studies of incompressible turbulence have shown the existence of a spectral bump, which is a precursor to the k^{-1} part of the scalar spectrum and becomes more and more pronounced as Sc increases. In our simulations, although it gets clearer when Sc grows, the bump is not as conspicuous as that observed in Ref. [31]. Similar to C_ϕ, the 1D OC constant, $C_{1\phi}$, is changed by both Sc and Re_λ. We find that C_ϕ and $C_{1\phi}$ approximately satisfy the relation $C_\phi = 5C_{1\phi}/3$, which can be obtained directly through Eq. (3.2).

When the Schmidt number is $\mathrm{Sc} \gg 1$, the energy spectrum decays quickly at wave numbers larger than η^{-1}, whereas the scalar spectrum remains excited at levels higher than the energy spectrum [32]. In this case, the scalar transfer to small scales is creased at the Batchelor scale η_B through molecular diffusion. The range $\eta^{-1} \ll k \ll \eta_B^{-1}$ is called the viscous-convective range, wherein the scalar spectrum obeys a k^{-1} power law as follows:

$$E_\phi(k) = B_\phi\langle\epsilon_\phi\rangle(\nu/\langle\epsilon\rangle)^{1/2}k^{-1}. \tag{3.3}$$

Here, the nondimensional coefficient B_ϕ is presumed to be universal [31,32], and the value is $3 \sim 6$ [33,34]. The nonlocality of the scalar transfer in wave-number space is essential for the generation of this viscous-convective range. Therefore, a sufficiently high Sc is required to observe the k^{-1} power law. In Fig. 4(a) we plot the compensated spectra of scalar according to the Batchelor variables in low-Re flows, as functions of $k\eta$. For the $\mathrm{Sc} = 25$ flow, a plateau representing the k^{-1} power law is observed in the range of $0.1 \leqslant k\eta \leqslant 0.3$ (gray region), and the crossover region occurs in $0.06 < k\eta < 0.1$. However, the k^{-1} power law disappears when Sc is reduced to 5. This reveals that, in the viscous-convective range, the scalar spectrum in the $\mathrm{Sc} \gg 1$ compressible turbulent mixing defers to the k^{-1} scaling given by the Batchelor theory, which was previously developed for incompressible turbulence.

On the other hand, when the Schmidt number is $\mathrm{Sc} \ll 1$, the scalar fluctuations at scales smaller than the OC scale, $\eta_{\mathrm{OC}} = \mathrm{Sc}^{-3/4}\eta$, decay strongly and, thus, the scalar spectrum rolls off steeper than the $k^{-5/3}$ power law. If the Reynolds number is sufficiently large, standard arguments suggest that, in the range of $\eta_{\mathrm{OC}}^{-1} \ll k \ll \eta^{-1}$, a so-called inertial-diffusive range exists. The aforementioned BHT theory predicts that, in this range, the scalar spectrum has the form

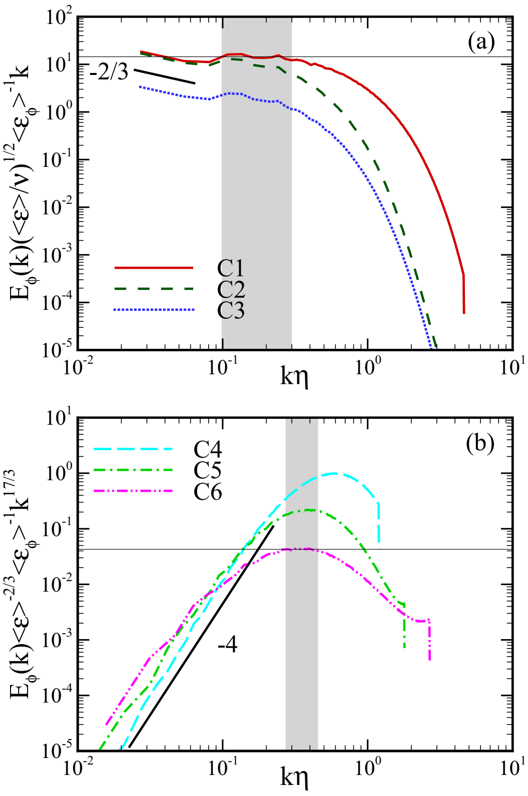

FIG. 4. (Color online) (a) Compensated spectrum of scalar according to the Batchelor variables at Sc = 25, 5, and 1 and low Re_λ, where the slope value of the short line is $-\frac{2}{3}$. (b) The same as panel (a) according to the Batchelor–Howells–Townsend variables at Sc = 1, $\frac{1}{5}$, and $\frac{1}{25}$ and high Re_λ, where the slope value of line is -4.

$$E_\phi(k) = (C_K/3)\langle\epsilon_\phi\rangle\langle\epsilon\rangle^{2/3}\chi^{-3}k^{-17/3}. \tag{3.4}$$

Figure 4(b) shows the compensated spectra of scalar according to the BHT variables in high-Re flows as functions of $k\eta$. We observe that, in the $\mathrm{Sc} = \frac{1}{25}$ flow, a narrow plateau representing the $k^{-17/3}$ power law arises, where the scale range is roughly $0.3 \leqslant k\eta \leqslant 0.4$ (gray region), which corresponds to $3.4 \leqslant k\eta_{\mathrm{OC}} \leqslant 4.5$. The above result demonstrates that, in the inertial-diffusive range, the scalar spectrum in the $\mathrm{Sc} \ll 1$ compressible turbulent mixing follows the $k^{-17/3}$ scaling provided by BHT theory.

The second-order structure function of scalar increment is defined by

$$S_{\phi 2}(r) \equiv \langle(\delta_r\phi)^2\rangle, \tag{3.5}$$

where $\delta_r\phi = \phi(\mathbf{x}+r) - \phi(\mathbf{x})$ is the scalar increment. In Fig. 5 we plot $S_{\phi 2}(r)$ normalized by the OC variables, as suggested in Eq. (3.1), as functions of the normalized separation distance r/η. It shows finite-width plateaus at large r/η. The scaling constants computed by the plateaus in low-Re flows are higher

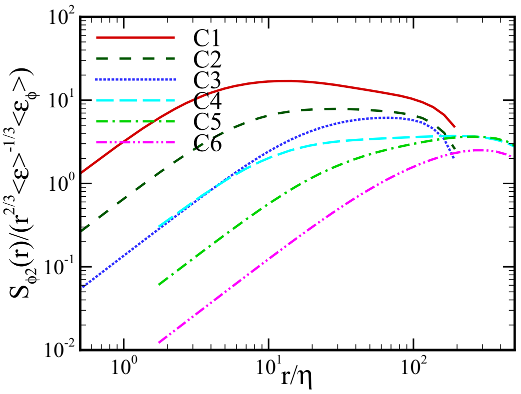

FIG. 5. (Color online) Obukhov–Corrsin scaling of second-order structure function of scalar at different values of Sc and Re_λ.

than those in high-Re flows. When Sc decreases, the values of scaling constants in both high- and low-Re flows become smaller. At sufficiently large scales, an asymptotic formulation obtained from incompressible turbulent mixing [31] gives

$$\frac{\langle(\delta_r\phi)^2\rangle}{\langle\epsilon_\phi\rangle\langle\epsilon\rangle^{-1/3}r^{2/3}} \approx \frac{3\mathrm{Re}_\lambda\mathrm{Sc}^{1/2}}{\sqrt{15}r_\phi}\left(\frac{r}{\eta_{\mathrm{OC}}}\right)^{-2/3}$$
$$= \frac{3\mathrm{Re}_\lambda}{\sqrt{15}r_\phi}\left(\frac{r}{\eta}\right)^{-2/3}. \tag{3.6}$$

Given that the scale range for a plateau is different in every case, in principle it explains the relative relations of the scaling constants in our simulations.

The mixed third-order structure function, defined as $S_{m3}(r) = \langle\delta_r u(\delta_r\phi)^2\rangle$, where $\delta_r u = u(\mathbf{x}+r) - u(\mathbf{x})$ is the longitudinal velocity increment, plays a more fundamental role in the similarity scaling. In incompressible turbulence, an exact result for $\eta_B \ll r \ll L_\phi$ was given by Yaglom [35]:

$$\langle\delta_r u(\delta_r\phi)^2\rangle = -\tfrac{4}{3}\langle\epsilon_\phi\rangle r. \tag{3.7}$$

Figure 6 presents the minus of $S_{m3}(r)$ normalized by the Yaglom variables. It is found that, for each simulated flow, there appears a flat region with finite width. Furthermore, in the limit of large scale, $-S_{m3}(r)$ drops quickly and approaches zero, while at small scales, it behaves approximately as r^2 according to the Taylor expansion. We now employ the quantity C_m to represent the compensated mixed third-order structure function:

$$C_m = -\frac{S_{m3}}{r\langle\epsilon_\phi\rangle}. \tag{3.8}$$

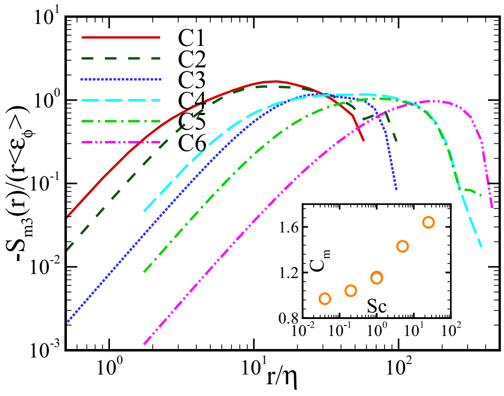

FIG. 6. (Color online) Yaglom scaling of mixed third-order velocity-scalar structure function at different values of Sc and Re_λ.

Our results show that, in flat regions, the scaling constant C_m is 1.64, 1.43, 1.15, 1.16, 1.04, and 0.97 from C1 through C6, respectively. Two aspects can thus be concluded: (1) the contribution from the variation in the Reynolds number to C_m is negligible, while the compressible effect makes C_m smaller than the $\frac{4}{3}$ value from incompressible turbulence, and (2) C_m has a tendency to increase with Sc, which is in agreement with the results shown in Ref. [31]. In the inset of Fig. 6 we plot C_m as a function of Sc.

B. Probability distribution function

Figure 7 shows the one-point PDF of the normalized scalar fluctuations. At small amplitudes the PDFs collapse to the Gaussian distribution, whereas at large amplitudes they decay more quickly than Gaussian and thus are known as sub-Gaussian. This feature corresponds to the passive scalar transport in 3D compressible and 1D incompressible turbulent flows [32,36], which is due to the fact that, in our simulations, the ratio of the integral length scale of scalar L_ϕ to the computational domain L_0 is $0.19 \sim 0.21$, which prevents large scalar fluctuations.

In Fig. 8 we plot the one-point PDF of the normalized scalar gradient, where $\zeta' = [\langle(\partial\phi/\partial x_j)^2\rangle]^{1/2}$ is the r.m.s. magnitude of the scalar gradient. Obviously, the convex PDF tails are much longer than those of the Gaussian, indicating strong intermittency. In both high- and low-Re flows, the PDF tails on each side become broader as Sc increases. Moreover, in the $\mathrm{Sc} = 1$ flows, the notable increase in Re_λ leads the PDF tails to be significantly wide. These observations imply that the growth in the Reynolds and Schmidt numbers will reinforce the events of extreme scalar oscillations at small scales.

As a further study, in Figs. 9(a) and 9(b) we plot the two-point PDFs of scalar increment against the normalized separation distances of $r/\eta = 1$ and 256, where $\sigma_{\delta\phi}$ is the standard deviation of $\delta\phi$. We find that, in both high- and low-Re_λ flows, the behavior of the PDF tails at large and

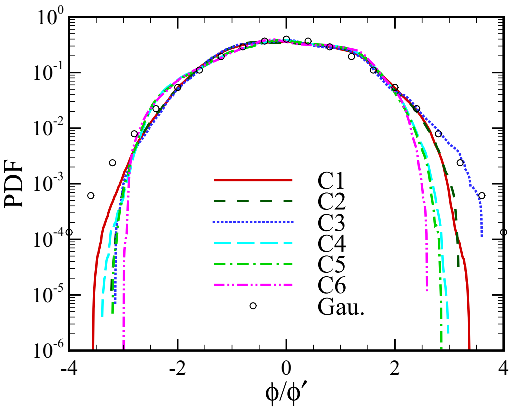

FIG. 7. (Color online) The one-point PDF of the normalized scalar fluctuations at different values of Sc and Re_λ, where the circles are for the Gaussian PDF.

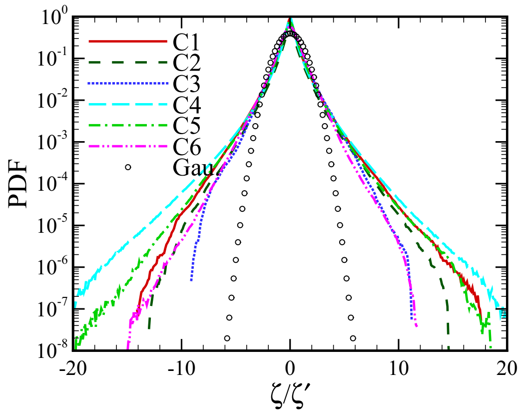

FIG. 8. (Color online) The one-point PDF of the normalized scalar gradient, where the circles are for the Gaussian PDF.

small scales are respectively similar to the one-point PDF tails shown in Figs. 7 and 8.

Many studies in the literature of incompressible turbulent flows suggest that, at small scales, the intermittency of the scalar field is closely associated with its dissipation. Figure 10 shows the PDFs of the normalized scalar dissipation rate, where $\epsilon'_\phi = [\langle(\epsilon_\phi - \langle\epsilon_\phi\rangle)^2\rangle]^{1/2}$ is the r.m.s. magnitude of ϵ_ϕ. Similar to that shown in Fig. 8, it is found that an increase in the Schmidt number strengthens the scalar dissipation occurring at large magnitudes.

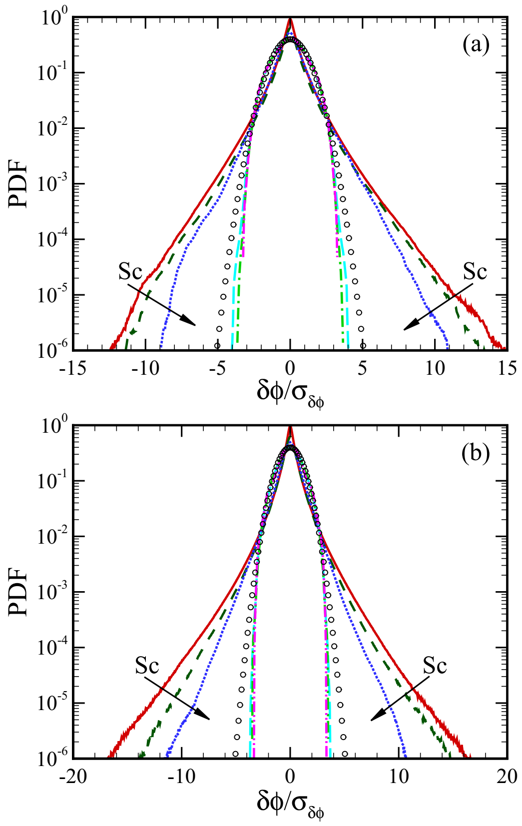

FIG. 9. (Color online) The two-point PDF of the normalized scalar increment. $(\mathrm{Sc}, r/\eta) = (25,1)$ for red solid line; $(\mathrm{Sc}, r/\eta) = (5,1)$ for black dashed line; $(\mathrm{Sc}, r/\eta) = (1,1)$ for blue dotted line; $(\mathrm{Sc}, r/\eta) = (25,256)$ for teal long dashed line; $(\mathrm{Sc}, r/\eta) = (5,256)$ for green dash-dotted line; and $(\mathrm{Sc}, r/\eta) = (1,256)$ for purple dash-dot-dotted line. The circles are for the Gaussian PDF, and the arrows indicate the decreasing Sc. (a) Low Reynolds number, (b) high Reynolds number.

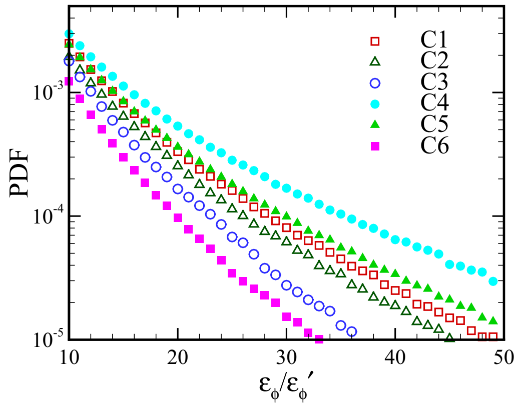

FIG. 10. (Color online) The PDF of the normalized scalar dissipation rate at different values of Sc and Re_λ.

C. Scalar transport analysis: High Sc versus low Sc

A central problem in turbulent mixing is the transport of scalar fluctuations in the inertial-convective range. For $\mathrm{Sc} \gg 1$ or $\mathrm{Sc} \ll 1$, this process should be also related to the viscous-convective or inertial-diffusive range. Figure 11

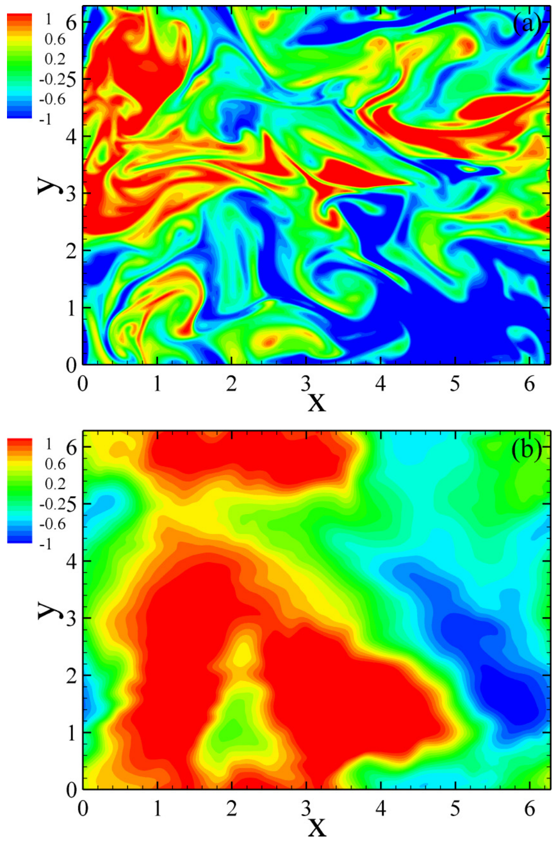

FIG. 11. (Color online) Two-dimensional contours of scalar field in (a) C1 and (b) C6, at $z = \pi/2$.

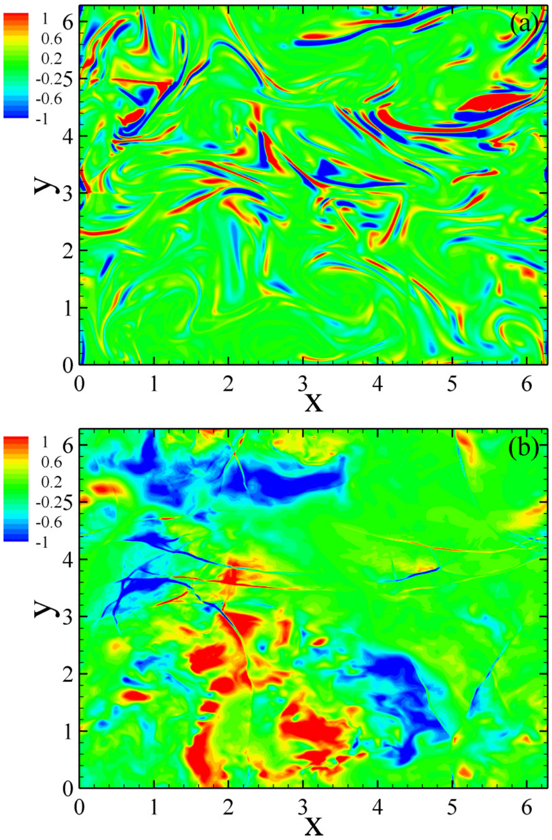

FIG. 12. (Color online) Two-dimensional contours of the advection term of the scalar variance equation in (a) C1 and (b) C6, at $z=\pi/2$.

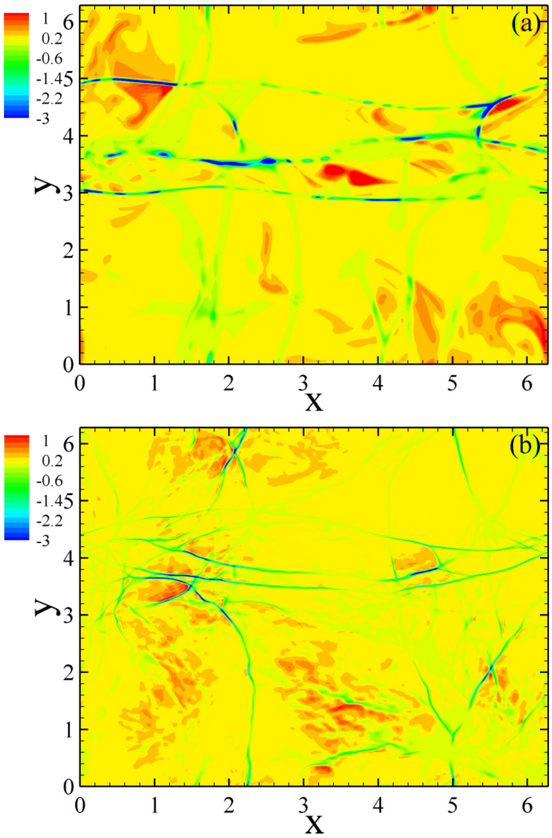

FIG. 13. (Color online) Two-dimensional contours of the scalar-dilatation term of the scalar variance equation in (a) C1 and (b) C6, at $z=\pi/2$.

shows the two-dimensional contours of scalar fields in the $z=\pi/2$ plane for the $\mathrm{Sc}=25$ and $\frac{1}{25}$ flows. In the highest Sc flow the low molecular diffusivity leads the scalar field to roll up and sufficiently mix. Nevertheless, in the lowest-Sc flow the scalar field loses the small-scale structures by the high molecular diffusivity and leaves the large-scale, cloudlike structures. Given that there are density fluctuations in compressible turbulence, we introduce the density-weighted scalar $\Phi=\sqrt{\rho}\phi$. The governing equation of scalar variance is then obtained by Eqs. (2.1) and (2.4) as follows:

$$\frac{\partial}{\partial t}\left(\frac{\Phi^2}{2}\right)=-u_j\frac{\partial}{\partial x_j}\left(\frac{\Phi^2}{2}\right)-2\theta\left(\frac{\Phi^2}{2}\right)-\frac{\chi}{\beta}\left(\frac{\partial\phi}{\partial x_j}\right)^2+\frac{\chi}{\beta}\frac{1}{\sqrt{\rho}}\frac{\partial^2}{\partial x_j^2}\left(\frac{\Phi^2}{2}\right). \tag{3.9}$$

Here, the terms on the right-hand-side of Eq. (3.9) successively stand for the advection, scalar-dilatation, dissipation, and diffusion. In statistically homogeneous turbulence, the global average on the diffusion makes it vanish. Therefore, in a statistically stationary state, we only focus the first three terms.

In Fig. 12 we present the two-dimensional contours of the advection terms in the $z=\frac{\pi}{2}$ plane for the $\mathrm{Sc}=25$ and $\frac{1}{25}$ flows. In the highest-Sc flow, the small-scale regions of extreme scalar advection distribute approximately randomly in space and display as thin streamers. For the lowest-Sc flow, the small-scale structures are basically smeared by the high molecular diffusivity and, thus, the remaining structures are large in scale and exhibited as clouds. Figure 13 shows the contours of the scalar-dilatation terms in the $z=\frac{\pi}{2}$ plane for the same flows. Because of the strong degree of compressibility induced by forcing, large-scale shock waves appear in the scalar-dilatation contours. Besides, in the vicinity of a shock front, the scalar undergoes drastic changes. To observe the detailed structures at both small and large amplitudes, in Fig. 14 we plot the logarithms of the dissipation term in the $z=\frac{\pi}{2}$ plane, where the color scale is determined as follows:

$$\psi=\log_{10}\left(D/D'\right). \tag{3.10}$$

Here, $D=\chi(\partial\phi/\partial x_j)^2/\beta$, and $D'=[\langle(D-\langle D\rangle)^2\rangle]^{1/2}$ is the r.m.s. magnitude of D. The color changes from blue to red when dissipation increases. In the highest-Sc flow, the contour shows that the extreme dissipation regions are sufficiently mixed and randomly distributed. In contrast, the high molecular diffusivity in the lowest-Sc flow leads the contour to retain only the large-scale cloudlike structures.

We now focus on the spectral analysis of the transport of scalar fluctuations. First, Eq. (3.9) in Fourier space is written as follows:

$$\hat{\Phi}^*(\mathbf{k})\frac{\partial}{\partial t}\hat{\Phi}(\mathbf{k})=-\hat{\Phi}^*(\mathbf{k})\widehat{\mathbf{u}\cdot\nabla\Phi}(\mathbf{k})-\hat{\Phi}^*(\mathbf{k})\widehat{\theta\Phi}(\mathbf{k})+\frac{\chi}{\beta}\hat{\Phi}^*(\mathbf{k})\widehat{\frac{1}{\sqrt{\rho}}\nabla^2\Phi}(\mathbf{k}), \tag{3.11}$$

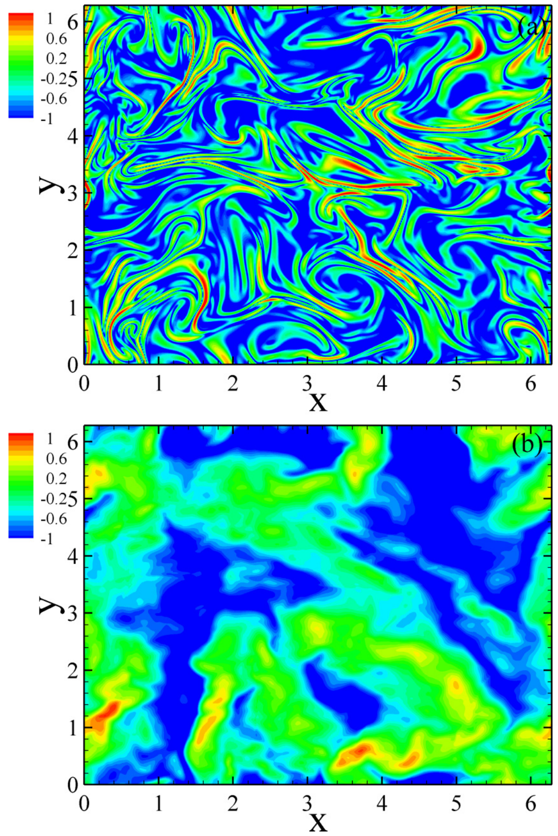

FIG. 14. (Color online) Two-dimensional contours of logarithm of the dissipation term of the scalar variance equation in (a) C1 and (b) C6, at $z = \frac{\pi}{2}$.

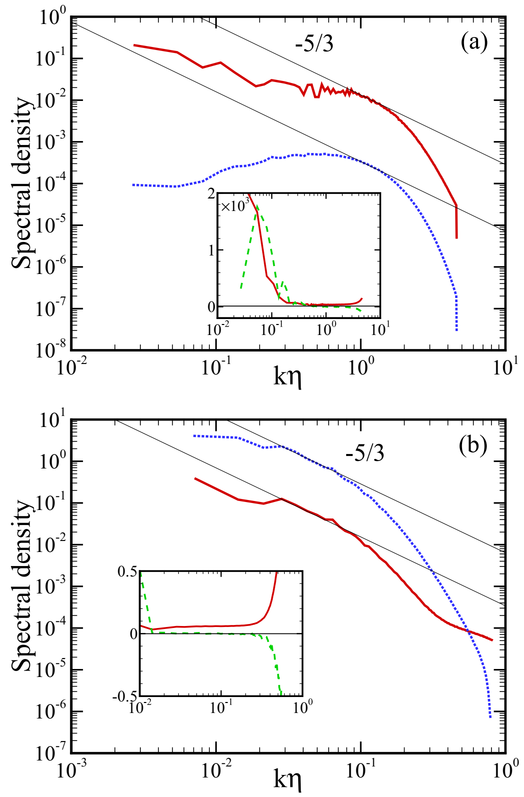

FIG. 15. (Color online) Spectral densities of terms in the scalar variance equation in Fourier space, where the solid and dotted lines are for the advection and dissipation terms, respectively. Inset: advection (solid line) and scalar-dilatation (dashed line) spectra normalized by the dissipation spectrum. (a) C1, (b) C6.

where the carets denote the Fourier coefficients, and the asterisks denote complex conjugates. In Fig. 15 we depict the log-log plots of the spectral densities of the advection and dissipation terms from Eq. (3.11). It is observed that in $\mathrm{Sc} = 25$ and $\frac{1}{25}$ flows, there appear $k^{-5/3}$ power laws for both advection and dissipation. This indicates that, although in compressible turbulent mixing, the presence of large-scale shock waves significantly affects the transport of scalar fluctuations, the processes of advection and dissipation may follow the Kolmogorov picture. Note that the process of scalar-dilatation coupling may not obey the Kolmogorov picture. The insets show the spectra of advection and scalar dilatation normalized by the dissipation spectrum. In the highest-Sc flow, both the advection and scalar-dilatation spectra fall quickly as wave number increases. In contrast, in the lowest-Sc flow the advection spectrum increases at large wave numbers; however, the scalar-dilatation spectrum is positive at small wave numbers but becomes negative at large wave numbers, indicating mutually opposing scalar transfer processes.

To determine the scalar spectra in both the highest- and lowest-Sc flows, we compute the compensated scalar spectra relative to the kinetic energy spectrum. According to the aforementioned theories, the results are $k^{-2/3}E_\phi/E_k$ at $\mathrm{Sc} = 25$ and k^4E_ϕ/E_k at $\mathrm{Sc} = \frac{1}{25}$. Figure 16 shows that plateaus appear for $k^{-2/3}E_\phi/E_k$ in the range of $38 \leqslant k \leqslant 51$ (gray region with dashed edge lines) and k^4E_ϕ/E_k in the range of $23 \leqslant k \leqslant 34$ (gray region with dash-dotted edge lines), respectively, which indicates that the related spectra defined in the viscous-convective and inertial-diffusive ranges have flat regions located at relatively large and small wave numbers, respectively. Undoubtedly, the kinetic-energy spectrum for both flows have the inertial range of $E_k(k) = C_k\langle\epsilon\rangle^{2/3}k^{-5/3}$ [21], where C_k is the Kolmogorov constant. This in turn yields E_ϕ as follows:

$$E_\phi \propto C_k\langle\epsilon\rangle^{2/3}k^{-1}, \quad \mathrm{Sc} = 25, \tag{3.12}$$

$$E_\phi \propto C_k\langle\epsilon\rangle^{2/3}k^{-17/3}, \quad \mathrm{Sc} = \tfrac{1}{25}. \tag{3.13}$$

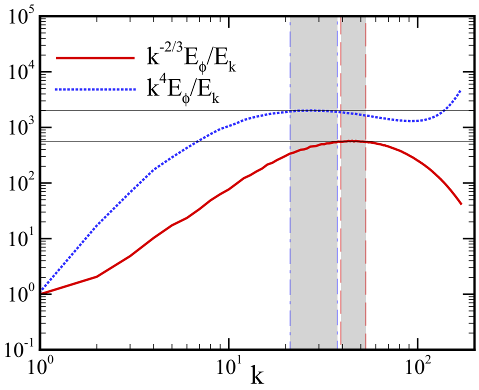

FIG. 16. (Color online) The relative compensated scalar spectra of $k^{-2/3}E_\phi/E_k$ and k^4E_ϕ/E_k in C1 and C6, respectively.

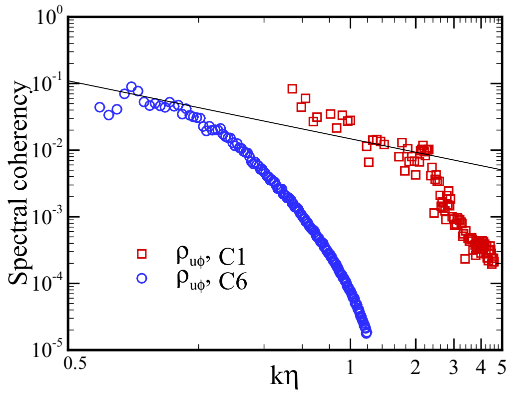

FIG. 17. (Color online) Spectral coherency of scalars in C1 and C6. The slope value of line is $-\frac{2}{3}$.

It is useful to work with the spectral coherency defined as

$$\rho_{u\phi}(k) \equiv E_{u\phi}(k)/[E_k(k)E_\phi(k)]^{1/2}. \tag{3.14}$$

Here, $E_{u\phi}(k)$ is the cospectrum of velocity and scalar, which is defined by [37]

$$E_{u\phi}(k) \equiv \int dS_k \langle u(\mathbf{k})\,\phi^*(\mathbf{k})\rangle, \tag{3.15}$$

where the integral $\int dS_k$ is taken over a spherical shell in wave-number space. Lumley [38] proposed a $k^{-7/3}$ power law for $E_{u\phi}(k)$ in the inertial-convective range, which was in good agreement with a recent simulation study [37]. Since both $E_k(k)$ and $E_\phi(k)$ scale as $k^{-5/3}$ under similar conditions, the corresponding result for $\rho_{u\phi}(k)$ must be $k^{-2/3}$. In Fig. 17, at high wave numbers, the spectral coherency in the $\mathrm{Sc} = 25$ and $\frac{1}{25}$ flows decay faster than $k^{-2/3}$. This deviation is mainly caused by the contribution from the coupling of scalar and dissipation, which provides a different power law. Contrary to the observations from incompressible turbulent mixing [15], here when Sc increases, the spectral coherency falls more slowly with wave number. Furthermore, the scattering of the spectral coherency points in the higher-Sc flow because of the lower Reynolds number.

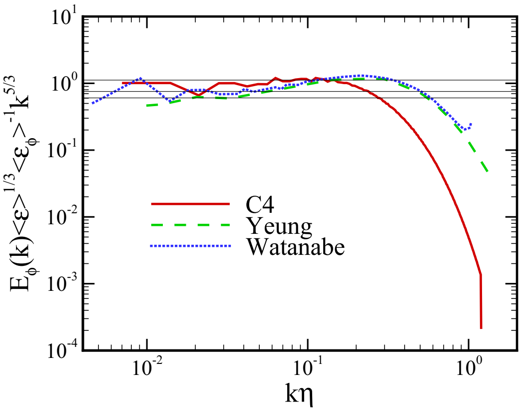

FIG. 18. (Color online) Compensated spectrum of scalar according to the Obukhov–Corrsin variables. The data from C4 and Refs. [31,32] are denoted by the solid, dashed, and dotted lines, respectively.

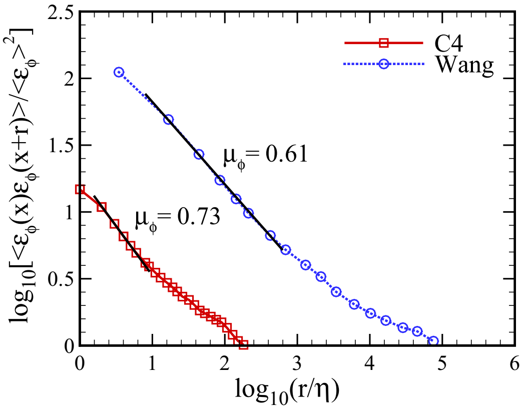

FIG. 19. (Color online) Autocorrelation of scalar dissipation rate, as a function of r/η, where the squares and circles are for the data from C4 and Ref. [30], respectively.

D. Comparison between compressible and incompressible results

In the final section we discuss the comparisons of certain results between compressible and incompressible turbulence. Herein, we focus solely on cases of Schmidt number at unity. In Fig. 18 we plot the compensated scalar spectra according to the OC variables from C4 and Refs. [31,32], where the values of Re_λ are 208, 240, and 258, respectively. For C4 the plateau centered at around $k\eta \approx 0.11$ gives $C_\phi \approx 1.12$. In contrast, the plateaus from the two incompressible flows are centered at lower wave numbers, and the values of C_ϕ are 0.67 ~ 0.68. The spectral bumps appearing in the two incompressible flows are quite conspicuous. However, in the compressible flow it is difficult to identify a clear bump. Furthermore, owing to the contribution of dissipation from shock waves, in the dissipative range, the scalar spectrum of compressible flow decays more quickly than its two incompressible counterparts.

Another discriminative issue involves the scalar intermittency in dissipative range. A commonly used method for quantifying this intermittency is to compute the so-called intermittency parameter μ_ϕ through the autocorrelation of scalar dissipation rate; namely,

$$\langle \epsilon_\phi(\mathbf{x})\,\epsilon_\phi(\mathbf{x}+\mathbf{r})\rangle \sim r^{-\mu_\phi}. \tag{3.16}$$

Figure 19 presents a log-log plot of the autocorrelations of ϵ_ϕ from C4 and Ref. [30] as functions of the normalized separation distance r/η. It shows that the values of μ_ϕ from the compressible and incompressible flows are 0.73 and 0.61, respectively. This means that, compared with its incompressible counterpart, the scalar dissipation field in the compressible turbulent mixing is more intermittent by virtue of the contribution from shock waves.

IV. SUMMARY AND CONCLUSIONS

In this paper, we systematically studied the effects of the Schmidt number on passive scalar transport in compressible turbulence. The simulations were solved numerically by adopting a hybrid approach of a seventh-order WENO scheme for shock regions, and an eighth-order CCFD scheme for smooth regions outside shocks. Large-scale predominant compressive forcing was added to the velocity field for reaching and maintaining a statistically stationary state. The simulated flows were divided into two groups. One was used to explore the scalar with low molecular diffusivity in low-Re flows, where the Schmidt number Sc was decreased from 25 to 1, and the Taylor microscale Reynolds number Re_λ was around 35. The other was addressed to the scalar with high molecular diffusivity in high-Re flows, where Sc was decreased from 1 to $\frac{1}{25}$, and Re_λ was around 210. Our results show that, in both groups, the ratio of the mechanical to scalar timescales increases as Sc decreases. As an alternative to r_ϕ, f_ϕ was found to fall monotonically when the product of Re_λ and Sc increases.

In the inertial-convective range of $L_\phi^{-1} \ll k \ll \eta^{-1}$, the scalar spectrum seems to obey the $k^{-5/3}$ power law, especially for the $\mathrm{Sc} = 1$ flows. Besides, the tendencies of the scalar spectra to grow and fall with wave numbers between the inertial-convective and dissipative ranges are reinforced by the increase and decrease in Sc, respectively. For the 1D scalar spectrum, the spectral bump becomes more visible as Sc increases, and the related OC constant and its 3D counterpart satisfy the relation $C_{1\phi} = 3C_\phi/5$. Furthermore, the scalar spectrum in the viscous-convective range of $\eta^{-1} \ll k \ll \eta_B^{-1}$ from the $\mathrm{Sc} = 25$ flow follows the k^{-1} power law, while that in the inertial-diffusive range of $\eta_{\mathrm{OC}}^{-1} \ll k \ll \eta^{-1}$ from the $\mathrm{Sc} = \frac{1}{25}$ flow shows a $k^{-17/3}$ scaling. At large scales, the scaling constant computed by the second-order structure function of scalar increment can be approximately described by using an asymptotic formulation developed for incompressible turbulence. Simultaneously, the one computed by the mixed third-order structure function of velocity-scalar increment shows that the dependence on the Reynolds number is negligible, and the effect of compressibility makes it smaller than the $\frac{4}{3}$ value from incompressible turbulence. In addition, this scaling constant has an increasing tendency when Sc grows.

At small amplitudes, the one-point PDF of scalar fluctuations collapses to the Gaussian distribution, whereas at large amplitudes it is sub-Gaussian, exhibiting a decay that is quicker than Gaussian. For the one-point PDF of scalar gradient, the convex PDF tails are much longer than Gaussian, indicating strong intermittency. In both high and low Re flows, the PDF tails on each side become broader as Sc increases. Furthermore, for the $\mathrm{Sc} = 1$ flows a notable increase in Re_λ leads the PDF tails to be significantly wide, implying that the growth in the Reynolds and Schmidt numbers will enhance the events of extreme scalar oscillations at small scales. At large scales, the behavior of the two-point PDF of scalar increment resembles the one-point PDF of scalar fluctuation, while at small scales, it is similar to that of scalar gradient. In terms of scalar dissipation, it occurs more at large magnitudes when Sc grows.

The contour shows that in the highest-Sc flow the scalar field rolls up and gets sufficiently mixed, whereas in the lowest Sc flow it loses the small-scale structures because of high molecular diffusivity, and leaves the large-scale, cloudlike structures. A further study on the contours of scalar advection and dissipation finds that in the highest-Sc flow, streamers with extreme values are small in scale and are distributed approximately randomly in space, whereas in the lowest-Sc flow only the large-scale, cloudlike structures exist. In certain ranges, the spectral densities of scalar advection and dissipation seem to have the $k^{-5/3}$ power law. This indicates that, for the transport of scalar fluctuations in compressible turbulent mixing, the advection and dissipation other than the scalar-dilatation coupling may follow the Kolmogorov picture. By computing the compensated spectra of scalar relative to the kinetic-energy spectrum, it is confirmed that the scalings of k^{-1} and $k^{-17/3}$ are defined for the scalar spectra in the viscous-convective and inertial-diffusive ranges, respectively. It then shows that, at high wave numbers, the magnitudes of spectral coherency in both the highest- and lowest-Sc flows decay faster than $k^{-2/3}$, which is not similar to the prediction from classical theory. Finally, the comparison with incompressible results displays that the scalar in the $\mathrm{Sc} = 1$ compressible flow lacks a conspicuous bump structure in its spectrum near the dissipative range; however, it is more intermittent in this range.

In summary, the above findings reveal that the change in the Schmidt number has pronounced influence on the small-scale statistics and field structure of passive scalar in compressible turbulence. Besides, although the turbulent Mach number used in the current study is not very high, the effect of compressibility still affects scalar mixing in certain respects. A deeper investigation on this topic under much higher Reynolds and Schmidt numbers will be carried out in the near future. Also, we will examine the effects of Mach number and forcing scheme on compressible turbulent mixing.

ACKNOWLEDGMENTS

The author thanks Dr. J. Wang for many useful discussions. This work was supported by the National Natural Science Foundation of China (Grants No. 91130001 and No. 11221061), and the China Postdoctoral Science Foundation Grant No. 2014M550557. Simulations were done on the TH-1A supercomputer in Tianjin, National Supercomputer Center of China.

---

[1] D. M. Meyer, M. Jura, and J. A. Cardelli, Astrophys. J. **493**, 222 (1998).
[2] S. I. B. Cartledge, J. T. Lauroesch, D. M. Meyer, and U. J. Sofia, Astrophys. J. **641**, 327 (2006).
[3] R. Lu and R. P. Turco, J. Atmos. Sci. **51**, 2285 (1994).
[4] R. Lu and R. P. Turco, Atmos. Environ. **29**, 1499 (1995).
[5] S. B. Pope, Symp. (Int.) Combust., [Proc.] **23**, 591 (1991).
[6] Z. Warhaft, Annu. Rev. Fluid Mech. **32**, 203 (2000).
[7] K. R. Sreenivasan, Phys. Fluids **8**, 189 (1996).
[8] L. Mydlarski and Z. Warhaft, J. Fluid Mech. **358**, 135 (1998).
[9] P. K. Yeung, D. A. Donzis, and K. R. Sreenivasan, Phys. Fluids **17**, 081703 (2005).
[10] P. L. Miller and P. E. Dimotakis, J. Fluid Mech. **308**, 129 (1996).

[11] D. Bogucki, J. A. Domaradzki, and P. K. Yeung, J. Fluid Mech. **343**, 111 (1997).
[12] D. A. Donzis and P. K. Yeung, Physica D **239**, 1278 (2010).
[13] G. K. Batchelor, J. Fluid Mech. **5**, 113 (1959).
[14] P. K. Yeung and K. R. Sreenivasan, J. Fluid Mech. **716**, R14 (2012).
[15] P. K. Yeung and K. R. Sreenivasan, Phys. Fluids **26**, 015107 (2014).
[16] G. K. Batchelor, I. D. Howells, and A. A. Townsend, J. Fluid Mech. **5**, 134 (1959).
[17] L. Pan and E. Scannapieco, Astrophys. J. **721**, 1765 (2010).
[18] L. Pan and E. Scannapieco, Phys. Rev. E **83**, 045302(R) (2011).
[19] J. Wang, L.-P. Wang, Z. Xiao, Y. Shi, and S. Chen, J. Comput. Phys. **229**, 5257 (2010).
[20] Q. Ni and S. Chen (unpublished).
[21] Q. Ni (unpublished).
[22] D. S. Balsara and C. W. Shu, J. Comput. Phys. **160**, 405 (2000).
[23] S. K. Lele, J. Comput. Phys. **103**, 16 (1992).
[24] R. Samtaney, D. I. Pullin, and B. Kosovic, Phys. Fluids **13**, 1415 (2001).
[25] Q. Ni, Y. Shi, and S. Chen, arXiv:1505.02685.
[26] A. N. Kolmogorov, Dokl. Akad. Nauk SSSR **30**, 9 (1941).
[27] A. N. Kolmogorov, Dokl. Akad. Nauk SSSR **32**, 16 (1941).
[28] A. M. Obukhov, Izv. Geogr. Geophys. **13**, 281 (1949).
[29] S. Corrsin, J. Appl. Phys. **22**, 469 (1951).
[30] L.-P. Wang, S. Chen, and J. C. Wyngaard, J. Fluid Mech. **400**, 163 (1999).
[31] P. K. Yeung, S. Xu, and K. R. Sreenivasan, Phys. Fluids **14**, 4178 (2002).
[32] T. Watanabe and T. Gotoh, New J. Phys. **6**, 40 (2004).
[33] R. H. Kraichnan, Phys. Fluids **11**, 945 (1968).
[34] R. H. Kraichnan, J. Fluid Mech. **64**, 737 (1974).
[35] A. M. Yaglom, Dokl. Akad. Nauk SSSR **69**, 6 (1949).
[36] Q. Ni and S. Chen, Phys. Rev. E **86**, 066307 (2012).
[37] T. Watanabe and T. Gotoh, Phys. Fluids **19**, 121701 (2007).
[38] J. L. Lumley, Phys. Fluids **10**, 855 (1967).